Energy Storage Materials 75 (2025) 104038

Contents lists available at ScienceDirect

Energy Storage Materials

journal homepage: www.elsevier.com/locate/ensm

Electroactive tetrathiafulvalene-based covalent organic framework with thiophene units as anode for high-performance hybrid lithium-ion capacitors
Dedicated to Professor Hong-Cai Zhou on the occasion of his 60th birthday

Zhi-Mei Yang [a,1], Yaoda Wang [a,1], Meng-Hang Zhang [a], Zhe-Yuan Hou [a], Shu-Peng Zhao [a], Xiao Han [a], Shuai Yuan [a], Jian Su [a,b,*], Zhong Jin [a,*], Jing-Lin Zuo [a,*]

[a] State Key Laboratory of Coordination Chemistry, MOE Key Laboratory of Mesoscopic Chemistry, MOE Key Laboratory of High Performance Polymer Materials and Technology, Jiangsu Key Laboratory of Advanced Organic Materials, Tianchang New Materials and Energy Technology Research Center, Institute of Green Chemistry and Engineering, School of Chemistry and Chemical Engineering, Nanjing University, Nanjing, Jiangsu, 210023, China
[b] School of Chemistry and Chemical Engineering, Nanjing University of Science and Technology, Nanjing, 210094, PR China

ARTICLE INFO

Keywords:
Electroactive covalent organic framework
Tetrathiafulvalene
Thiophene unit
Hybrid lithium-ion capacitor

ABSTRACT

Enhancing the performance of hybrid lithium-ion capacitors (HLICs) by regulating the structural characteristics of covalent organic frameworks (COFs) has been a challenge. In this study, electron-rich thiophene units combining with the electroactive tetrathiafulvalene (TTF) motif consists the designable organic linker, tetrathiafulvalene tetrathiophenal (TTFTTA). A novel 2D COF, TTFTTA-PDA (PDA, *p*-phenylenediamine), was assembled via a solvothermal method. TTFTTA-PDA exhibits reversible redox activity, a large Brunauer−Emmett−Teller surface area (457 $m^2 g^{-1}$) and high stability (pH 3~14). Furthermore, compared with the reported tetrathiafulvalene-tetrabenzaldehyde (TTFTBA)-based COF, TTFTBA-PDA, the introduction of thiophene rings enhances the capability of electron transfer, characterized by a smaller band gap (1.45 eV) and a lower calculated energy gap (0.89 eV). As a result, the electrochemical performance of TTFTTA-PDA in HLICs is outstanding. In the full-cell configurations, TTFTTA-PDA||activated carbon HLICs exhibit impressive energy density (140 Wh kg^{-1} at 233 W kg^{-1}), power density (9328 W kg^{-1} at 91 Wh kg^{-1}), and cycling lifespan (the capacity retention of 81.3 % after 2200 cycles), demonstrating a certain level of competitiveness among the reported state-of-the-art HLICs utilizing metal organic framework-/COF-based anode materials. These results illustrate that the precise structural design of pristine COFs can be an effective strategy to enhancing the performance of HLICs.

1. Introduction

Hybrid lithium-ion capacitors (HLICs), combining a Faradaic battery electrode with a capacitive electrode, not only inherit the high energy density of the Faradaic battery electrode, but also exhibit high power performance and an exceptionally long cycle life attributed to the capacitive electrode. Consequently, they have emerged as a prominent energy storage device in recent years [1–3]. However, current hybrid capacitors encounter challenges in bridging the kinetic and lifespan gap between capacitor-type and battery-type electrodes, making it difficult to achieve the ultimate goal of high energy density comparable to lithium ion batteries [4–7]. The dynamics of traditional battery-type electrode materials (e.g., Co_3O_4, RuO_x) are significantly poorer than that of capacitor-type electrodes due to accompanying physical desorption/adsorption processes [4]. Therefore, there is a need to develop novel materials with sufficient Li^+ storage sites and fast kinetics to address these imbalances in HLICs.

Covalent organic frameworks (COFs), composed of customizable organic building blocks, possess the merits of structural designability, controlled porosity, high surface area and remarkable stability, making them promising candidates for electrode materials in HLICs. These characteristics enable the realization of high energy density, fast redox

* Corresponding authors.
E-mail addresses: sujian@njust.edu.cn (J. Su), zhongjin@nju.edu.cn (Z. Jin), zuojl@nju.edu.cn (J.-L. Zuo).
[1] These authors contributed equally to this work.

https://doi.org/10.1016/j.ensm.2025.104038
Received 13 November 2024; Received in revised form 24 December 2024; Accepted 13 January 2025
Available online 16 January 2025

kinetics and good stability in electrode materials [8–13]. Notably, the use of highly conductive 2D COF polyporphyrin (TThPP) as an electrode material marks the first time COFs have been investigated for applications in anode materials [14]. Among these, TTF-based COF, TTFTBA-PDA and their CNT composite anodes exhibit ultrahigh specific capacity (609 mAh g^{-1} at 100 mA g^{-1}) and outstanding power density (12 000 Wkg^{-1} at 4000 mA g^{-1}) [15]. The excellent performance can be attributed to the core electron-donating and redox-active TTF units, which provide abundant active sites and high charge conductivity for reversible Li^+ storage [15–20]. Meanwhile, poly(thiophene) with reversible redox behavior has been reported for using as an anode material [21–23]. However, the low redox activity and poor rate performance for poly(thiophene)-based anode limit its further development. Further research is needed to incorporate thiophene motifs into organic building blocks and construct COFs to enhance anode performance in HILCs.

Herein, a novel two-dimension TTFTTA-PDA COF, containing the TTF core and thiophene motif, was intentionally synthesized by combining tetrathiafulvalene tetrathiophenal (TTFTTA) and *p*-phenylenediamine (PDA). The reversible redox activity, large Brunauer−Emmett−Teller surface area and high stability of TTFTTA-PDA were confirmed by the solid-state cyclic voltammetry (CV), N_2 adsorption, powder X-ray diffraction (PXRD) and thermogravimetric analysis (TGA). Moreover, the solid-state UV-vis-NIR absorption spectra, electron paramagnetic resonance (EPR), and theory calculation were conducted to study the electron-transfer ability of TTFTTA-PDA. The slight improvement in the structure of TTFTBA-PDA enhanced the anode performances, resulting in a capacity of 224.9 mAh g^{-1} at 2000 mA g^{-1} in half batteries, more than twice of TTFTBA-COFs. TTFTTA-PDA also exhibited high energy density of 140 Wh kg^{-1} at 233 W kg^{-1}, power density of 9328 W kg^{-1} at 91 Wh kg^{-1}, and outstanding stability with 81.3 % capacity retention after 2200 cycles as anode materials in full-cell HLICs. This work provides an example of using designed COF material composed by targeted organic building blocks with significant activity, porosity, high surface area and excellent stability to improve the overall performance as an anode electrode in HLICs, and is expected to inspire future research efforts in this area.

2. Results and discussion

2.1. Synthesis and structural characterizations

TTFTTA was prepared according to the reported methods (Fig. S1) [24]. In addition, the single-crystal structure of TTFTTA was clearly illustrated (Fig. S2). TTFTTA-PDA COF was synthesized through the condensation reaction between TTFTTA and *p*-phenylenediamine in mixtures of orthodichlorobenzene/AcOH (10:1, by volume) at 120°C for 7 days (Fig. 1a). PXRD analysis was conducted to confirm the structure of TTFTTA-PDA through combining with structural simulation using Materials Studio. The yellow curve obtained from Pawley refinements matched well with the experimental data represented by the black dots, as indicated by their negligible differences shown in the green curve. TTFTTA-PDA exhibits one intense peak at 5.67° and relatively weak peaks at 7.73°, 11.38°, 24.69°, and 27.28°, corresponding to the (110), (130), (220), (001), and (111) facets, respectively (Fig. 1d). Pawley refinement of TTFTTA-PDA based on a *C*222 orthorhombic space group provided lattice parameters of a =16.60, b = 45.61, and c = 3.60 Å. This structure adopts a 2D ***sql*** net with an eclipsed AA-stacking mode (Fig. 1b). The smallest S…S distance between adjacent planes is 3.6 Å, which is lower than previously reported TTF-based TTFTBA-COF with the value of 4.3 Å (Fig. S3). Meanwhile, the refinement results matched the experimental data with good agreement factors (Rp = 2.51 % and Rwp = 3.15 %). It is worth mentioning that the COF model was also simulated using the ligand in its original configuration from the single crystal. However, the simulated model under primary configuration could not correspond with the experimental data (Fig. S4). Fourier transform infrared (FT-IR) spectroscopy was used to further confirm the successful formation of TTFTTA-PDA-COF. A new peak at 1616 cm^{-1} was observed for TTFTTA-PDA, which is ascribed to the formation of the C=N bond [25,26]. The concomitant disappearances of the N−H stretching vibration (3200−3400 cm^{-1} for PDA) and the C=O stretching vibration (1653 cm^{-1} for TTFTTA) also indicated the complete conversion of amine and aldehyde groups (Fig. 1e) [26,27]. The formation of the C=N bond were further confirmed by recording the cross-polarization magic angle spinning ^{13}C nuclear magnetic resonance (CP-MAS^{13}C NMR) spectrum of TTFTTA-PDA solid. (Fig. S5) [28,29]. The designed TTFTTA-PDA exhibits cluster-like morphology, as evidenced by high-resolution transmission electron microscopy (HRTEM) and scanning electron microscopy (SEM), and the aggregation of smaller crystallites resulted in ambiguous crystal morphology (Fig. 1h and S6). Additionally, the corresponding elemental mapping analyses showed that carbon, nitrogen, and sulfur is uniformly distributed over TTFTTA-PDA, indicating homogeneous (Fig. 1i and S6). BET measurement was conducted to investigate its porosity. The isotherm of TTFTTA-PDA showed a significant uptake in the low-pressure region ($P/P_0<0.1$) and the calulated BET surface area was up to 457 m^2 g^{-1} (Fig. 1f). Pore size distribution was futher obtained through the adsorption isotherm, revealing that the pore size of TTFTTA-PDA is 11 Å, which is similar to the value of its theoretical calculation (12 Å). To study the chemical stability of TTFTTA-PDA COF, PXRD experiments were performed after immersion in different organic solvents and water over a wide pH range (pH 3∼14) for 24 h and the results reveal that the main structure is preserved (Fig. 1g and S7). TGA was conducted on TTFTTA-PDA, and the relevant curve revealed that the frameworks possess good thermal stability up to 330°C (Fig. S8).

2.2. Electrical properties of TTFTTA-PDA COF

The TTF core is well-known as an electron donor. The redox activity of both TTFTTA and TTFTTA-PDA was investigated through solid-state CV measurements. The experiments were conducted in 0.1 M $LiBF_4$ in CH_3CN. Upon scanning anodically, two *quasi*-reversible one-electron processes were clearly observed, ascribed to the $TTF/TTF^{\bullet+}$ and $TTF^{\bullet+}/TTF^{2+}$ redox couples. For TTFTTA, these reversible processes appeared at 0.26 and 0.56 V (vs. Fc/Fc^+), while for TTFTTA-PDA, they appeared at 0.31 and 0.57 V (vs. Fc/Fc^+) (Fig. 2a). In comparison to TTFTTA, both oxidation steps for TTFTTA-PDA are shifted to higher potentials, similar to what has been observed in reported TTF-COF based on tetrathiafulvalene-tetrabenzaldehyde (TTFTBA) [30]. Furthermore, the observed potential values are smaller than those of TTFTBA-COF but larger than those of TTF carboxylate-based MOFs [31–33]. Additionally, faster sweep rates resulted in broader features due to slow diffusion kinetics through the framework structure (Figs. S9 and S10).

In the solid-state absorption spectra, both TTFTTA and TTFTTA-PDA exhibited strong absorbance in the wavelength range of 300 to 650 nm, corresponding to the $n \rightarrow \pi^*$ or $\pi \rightarrow \pi^*$ transitions of TTFTTA [33–35]. Moreover, the band gaps based on Tauc plots for TTFTTA and TTFTTA-PDA are approximately 1.41 and 1.45 eV, respectively (Fig. 2b and S11). These values are significantly smaller than those of the reported neutral TTF-based MOFs, indicating that the electron transitions are more favorable in TTFTTA-PDA [35–37].

EPR measurements were conducted on TTFTTA and TTFTTA-PDA. An evident EPR signal with rhombic anisotropy at g = 2.005 (Fig. 2c) observed on TTFTTA-PDA. This signal can be attributed to the S = 1/2 $TTF^{\bullet+}$ species generated by intermolecular charge transfer between the linkers [16,35]. The close S···S interactions (with a distance of 3.6 Å between adjacent planes) revealed by the simulative structure of TTFTTA-PDA are beneficial for facilitating charge transfer. The electrical conductivity of TTFTTA-PDA, measured on pelletized sample at room temperature, was determined to be 1.05×10^{-5} $S{\cdot}m^{-1}$ (Fig. 2d and Table S1). This value agrees with the electrical conductivities of powder TTF-based COFs [25,38]. Though the electrical conductivity of

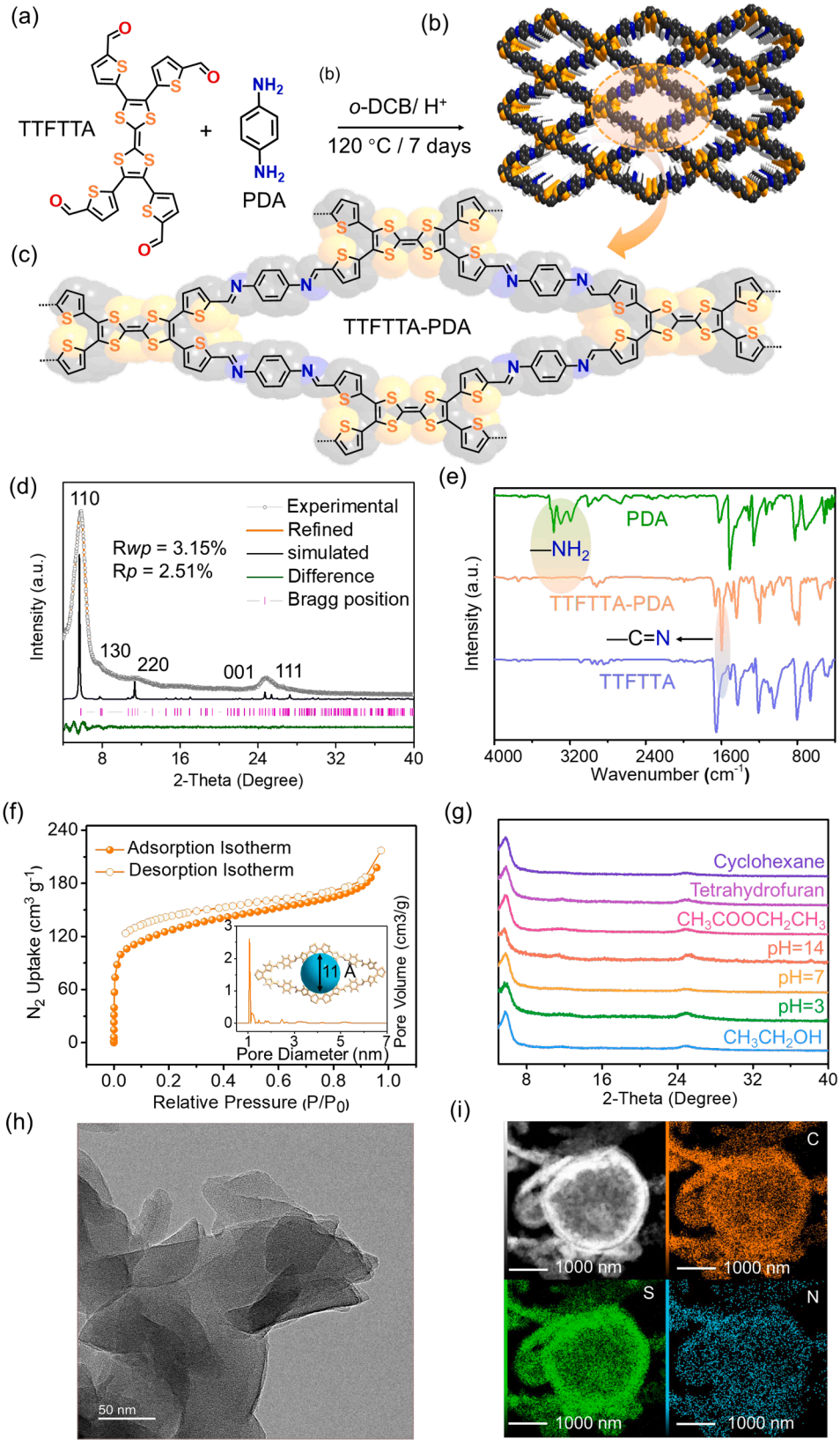

Fig. 1. Synthesis and structural characterizations of TTFTTA-PDA COF. (a) Synthesis of TTFTTA-PDA. (b) Extended structures of mesoporous 2D TTFTTA-PDA COF. Color scheme: O, red; C, dark gray; S, yellow. (c) The unit structure of TTFTTA-PDA COF. (d) Experimental and simulated PXRD patterns of TTFTTA-PDA, with the experimental profiles in gray, the Pawley refined profiles in orange, the simulated profiles (from the refined structure model) in black, the differences between experimental and refined PXRD patterns in green, and the Bragg positions in pink. (e) FT-IR spectra of TTFTTA-PDA and the corresponding building units. (f) The plots of N_2 adsorption isotherm measured at 77 K. The inset picture represents pore-size distribution profile for TTFTTA-PDA. (g) Observed powder X-ray diffraction patterns for TTFTTA-PDA at different solvent conditions. (h) TEM image of TTFTTA-PDA COF. (i) Element mapping images of TTFTTA-PDA COF.

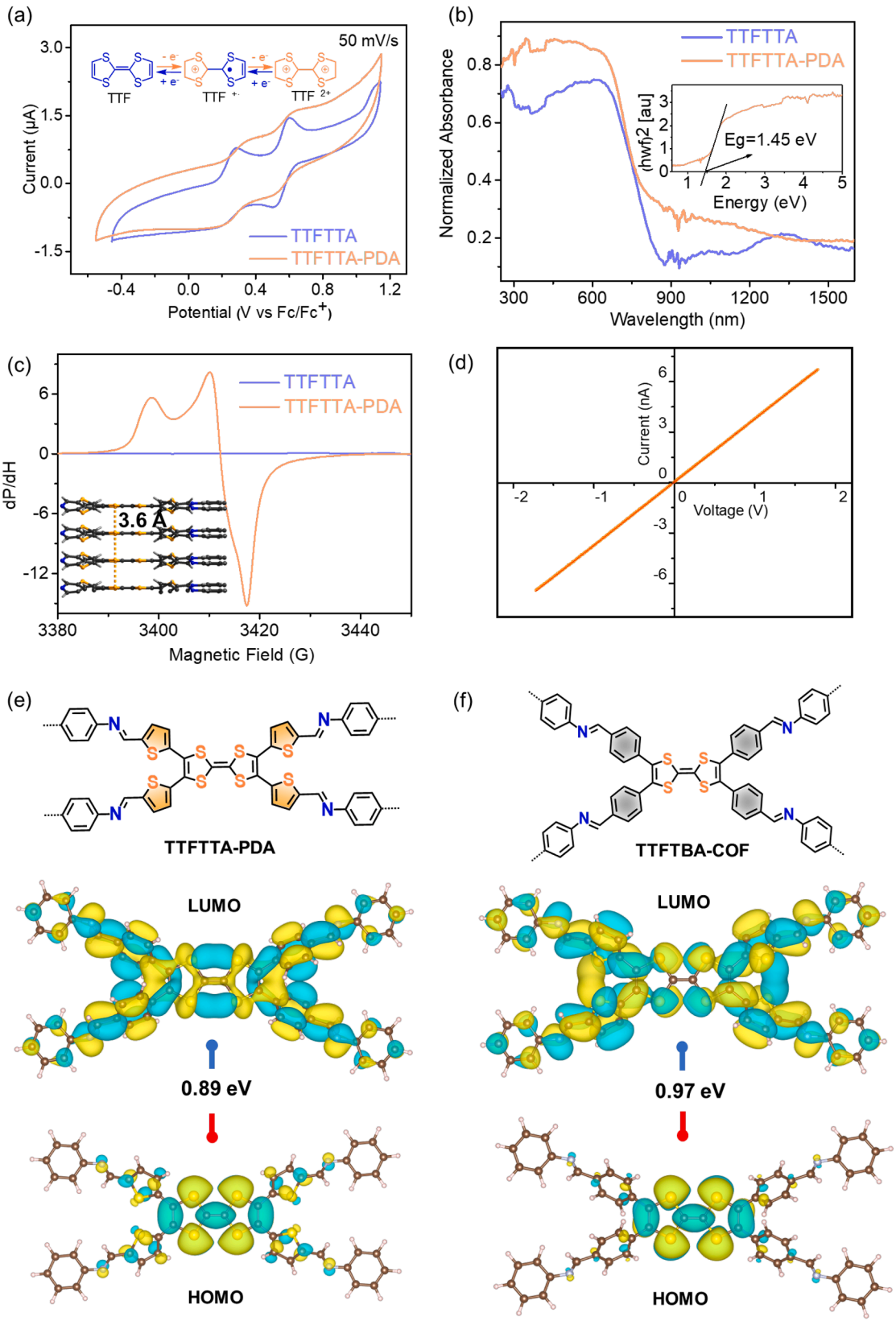

Fig. 2. Basic and electrical properties of TTFTTA-PDA COF. (a) Solid-state cyclic voltammograms of TTFTTA and TTFTTA-PDA performed at the scan rate of 50 mV/s in 0.1 M $LiBF_4$ in MeCN. (b) The solid-state UV-vis-NIR absorption spectra of TTFTTA and TTFTTA-PDA. The inset picture is the Tauc plot of TTFTTA-PDA. (c) The solid-state electron paramagnetic resonance spectra of TTFTTA and TTFTTA-PDA. The inset picture shows the S…S distance between adjacent planes. (d) I-V curve of TTFTTA-PDA. (e) HOMO and LUMO orbital distribution analyses and their calculated energy gap in TTFTTA-PDA. (f) HOMO and LUMO orbital distribution analyses and their calculated energy gap in TTFTBA-COF.

TTFTTA-PDA is not as excellent as expected, possibly due to the high contact resistance [31,39], it is improved obviously compared with TTFTBA-COF, which is calculated to be 3.96×10^{-6} S·m^{-1} (Fig. S12 and Table S1). Through HOMO and LUMO orbital distribution analyses and calculations of their energy gaps, we further confirmed that electrons become more easily transportable when the benzene ring is replaced by a thiophene ring. In TTFTTA-PDA, the ΔE is 0.89 eV, while in TTFTBA-COF, it is 0.97 eV (Fig. 2e and Table S2). Particularly, the HOMO and LUMO orbital distribution analysis and calculation for energy gaps of ligand were also conducted (Fig. S13). The results are consistent with the calculated band gaps based on Tauc plots. Additionally, we further apply TTFTTA-PDA in lithium-ion capacitors due to its electroactive properties.

2.3. Electrochemical properties of TTFTTA-PDA-COF

To investigate the electrochemical performance of TTFTTA-PDA, TTFTTA-PDA||Li half batteries were assembled with copper (Cu) foils loaded with TTFTTA-PDA active materials as working electrodes and Li foils as counter electrodes. CV analysis based on TTFTTA-PDA||Li half batteries was performed at a scan rate of 0.5 mV s^{-1} between 0.001 and 3.0 V versus Li/Li$^+$ (*vs.* Li/Li$^+$). As shown in Fig. 3a, the signal peak appearing at ~0.5 V during the first negative sweep disappeared in the subsequent cycles, which was mainly attributed to the formation of SEI by the decomposition of carbonate electrolytes. From the second cycle, the broad anodic and cathodic peaks in CV curves indicated the Li$^+$ storage behavior with an insertion/extraction mechanism for TTFTTA-PDA anodes. In the TTFTTA-PDA molecular structure, the active sites for Li$^+$ storage included thiophene rings, C=N bonds, pore channels, and interlamination space, leading to a large specific capacity of TTFTTA-PDA anodes. Notably, the CV curves of the third and fifth cycles overlapped well with that of the second cycle, illustrating the high reversibility of Li$^+$ insertion/extraction for the TTFTTA-PDA anodes. Electrochemical impedance spectroscopy (EIS) measurements were

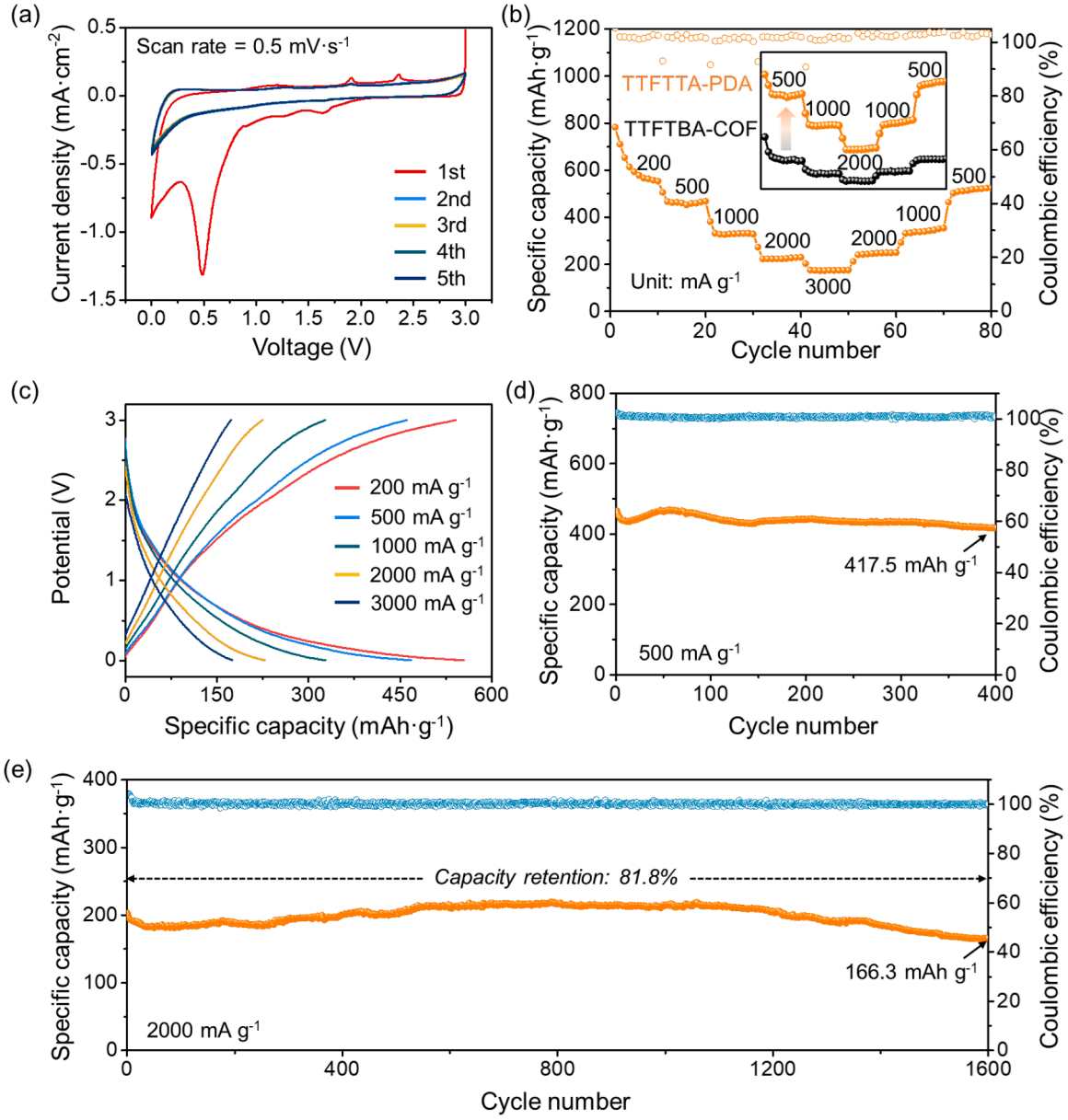

Fig. 3. Electrochemical performance of TTFTTA-PDA anodes. (a) CV curves of TTFTTA-PDA anodes at a scan rate of 0.5 mV s^{-1}. (b) Rate performance of TTFTTA-PDA anodes at different current densities from 200 to 3000 mA g^{-1}. (c) Galvanostatic charge/discharge curves of TTFTTA-PDA anodes at different current densities from 200 to 3000 mA g^{-1}. (d, e) Long-term cycling stability of TTFTTA-PDA anodes at the current densities of (d) 500 mA g^{-1} and (e) 2000 mA g^{-1}.

performed to further explore the mass-transfer kinetics of TTFTTA-PDA anodes (Fig. S14). After 20 cycles, TTFTTA-PDA||Li half batteries exhibited a much smaller interfacial impedance compared with that at the initial stage, suggesting the achievement of rapid charge transfer during the electrochemical process.

Fig. 3b displayed the rate performance of TTFTTA-PDA anodes at different current densities from 200 to 3000 mA g^{-1}. TTFTTA-PDA||Li half batteries delivered considerable discharge capacities of 577.9, 459.8, 330.8, 224.9, and 174.6 mAh g^{-1} with the increase of current densities of 200, 500, 1000, 2000, and 3000 mA g^{-1}, respectively. When the current density returned to 500 mA g^{-1}, the batteries delivered the well-recovered discharge capacity of 520.5 mAh g^{-1}, demonstrating the superior cycling reversibility and reaction kinetics of TTFTTA-PDA anodes. It is noticeable that the performance of TTFTTA-PDA are enhanced as the introduction of thiophene motifs [15], while TTFTBA-PDA only shows reversible capacity of 275.2 mAh g^{-1} to 84.7 mAh g^{-1} under current densities of 200 to 2000 mA g^{-1}. Moreover, it was noted that the galvanostatic charge/discharge curves of TTFTTA-PDA||Li half batteries at different current densities exhibited sloping trends (Fig. 3c), which verified the pseudocapacitive property of TTFTTA-PDA anodes. To examine the long-term cycling stability of TTFTTA-PDA anodes, TTFTTA-PDA||Li half batteries were cycled at the current density of 500 mA g^{-1} (Fig. 3d). At the initial stage, the specific discharge capacity was up to 466.3 mAh g^{-1}. After 400 cycles, the batteries could still deliver a remaining capacity of 417.5 mAh g^{-1}, corresponding to a capacity retention of 89.5 %. When cycled at a higher

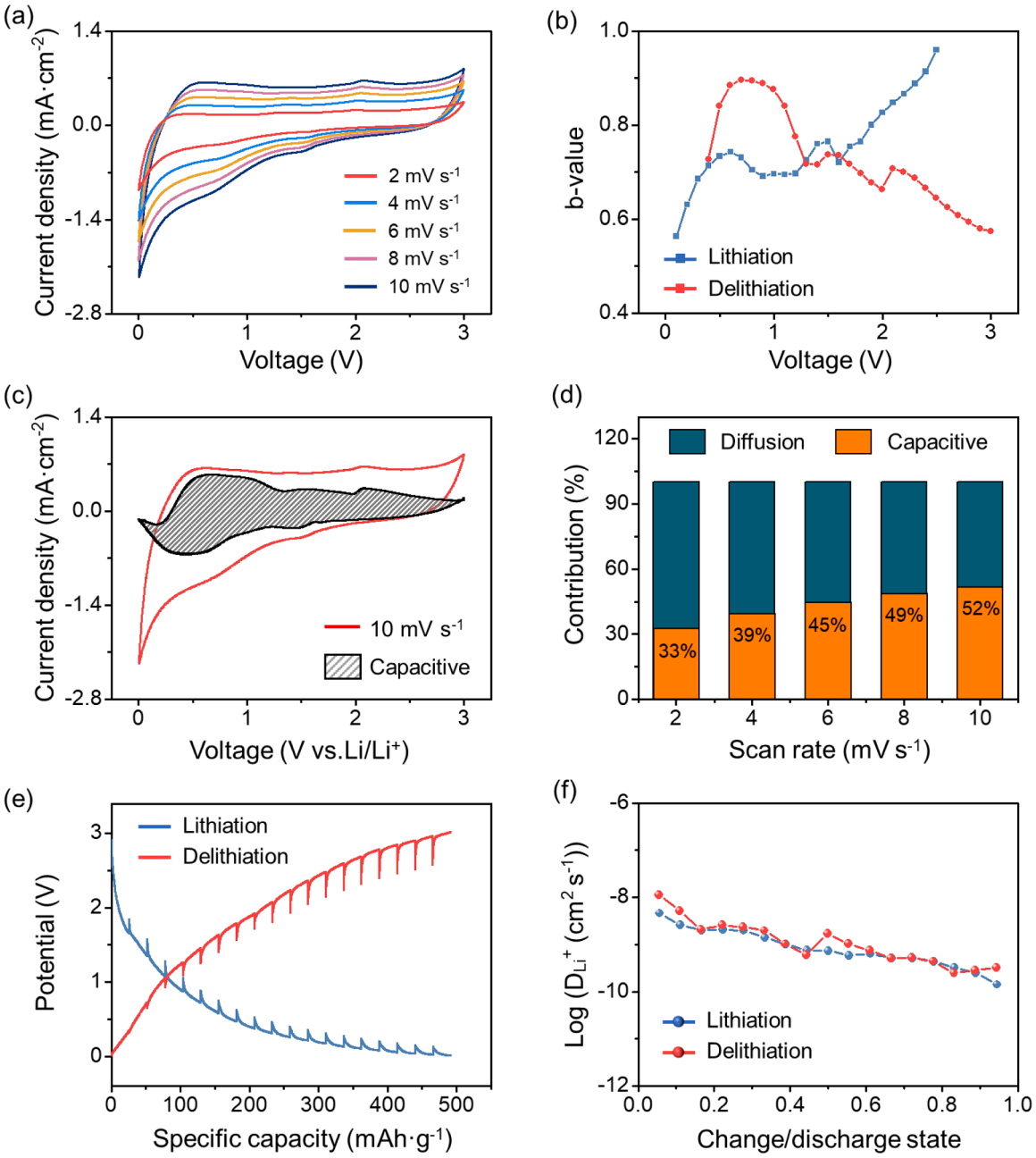

Fig. 4. Electrochemical kinetics properties of TTFTTA-PDA anodes. (a) CV curves of TTFTTA-PDA anodes at various scan rates from 2.0 to 10.0 mV s^{-1}. (b) Calculated *b*-values as a function of voltage for the cathodic and anodic processes. (c) CV curves of TTFTTA-PDA anodes at a scan rate of 10.0 mV s^{-1}. The capacitive contribution is marked by the grey shaded region. (d) Normalized contribution ratios of the pseudocapacitive process to the total capacity at different scan rates. (e) GITT curves of TTFTTA-PDA anodes at a constant current density of 20 mA g^{-1} with a relaxation time of 30 mins. f) Logarithm of the calculated Li^+ diffusion coefficients for lithiation and delithiation processes.

current density of 2000 mA g^{-1} (Fig. 3e), TTFTTA-PDA||Li half batteries also performed well. An initial discharge capacity of 203.2 mAh g^{-1} was achieved and an appreciable capacity retention of over 81.8 % was delivered even after 1600 cycles. It is worth noting that the activation process of porous materials has been exhibited in the first few hundred cycles, ascribed to the exposure of more active sites during the cycling process [16,40]. The above test results on rate performance and cycling stability strongly confirmed the high competitiveness of TTFTTA-PDA anodes, which mainly ascribed to TTFTTA-PDA as an active material with abundant active sites for Li^+ storage and superior electrochemical kinetics. To verify the structural integrity of TTFTTA-PDA, a series of spectroscopic characterizations were performed before and after cycling. In the XRD pattern of the cycled TTFTTA-PDA (Fig. S15), the characteristic peak at 5.67° corresponding to the (110) plane of TTFTTA-PDA, was observed after 10 cycles, indicating its well-maintained crystal structure. Moreover, superior electrochemical stability of TTFTTA-PDA was also demonstrated by the test results of FT-IR and Raman spectra. As displayed in Figs. S16 and S17, the cycled TTFTTA-PDA exhibited almost identical characteristic peaks as before cycling, confirming the stability of molecular structure after repeated Li plating/stripping cycles. To further specify the state of TTFTTA-PDA before and after long-term cycling, SEM investigation was conducted to characterize the surface morphology of TTFTTA-PDA anodes before and after 400 cycles. As shown in Fig. S18, almost no changes in surface morphology were observed for the TTFTTA-PDA anodes after cycling. EDX analysis also demonstrated the uniform distribution of components (Figs. S19 and S20), further verifying the stability of composition and structure for the TTFTTA-PDA anodes even after experiencing a long-term cycling process.

To further reveal the charge-storage kinetics and understand Li^+ storage mechanism of TTFTTA-PDA anodes, a series of electrochemical measurements were conducted systematically. By testing CV curves of TTFTTA-PDA||Li half batteries at various scan rates from 2.0 to 10.0 mV s^{-1} (Fig. 4a), the *b*-value was calculated to distinguish the capacitive behavior and diffusion-controlled process. The *b*-value could be determined by plotting the logarithm of current response (log*i*) versus the logarithm of scan rate (log*v*) (Fig. S21). The *b*-value of 0.5 indicated that the electrode kinetics was controlled by a semi-infinite diffusion process, while the surface capacitive behavior dominated the electrochemical process when the *b*-value approached 1.0. As shown in Fig. 4b, the *b*-values varied with the charge/discharge states, illustrating different capacitive contributions during the lithiation/delithiation process. When inserting Li^+ in the TTFTTA-PDA anodes, the *b*-value decreased from 0.96 (2.5 V *vs.* Li/Li^+) to 0.71 (0.4 V *vs.* Li/Li^+), indicating the electrochemical process within this voltage range was dominated by the surface capacitive behavior. When further discharging to 0.1 V, the *b*-value decreased to 0.56 (0.1 V *vs.* Li/Li^+), indicating the electrochemical process shifted towards diffusion control. The *b*-values for the delithiation process are demonstrated to be among 0.64 and 0.80, which indicated that both capacitive and diffusion-controlled processes contributed to the total capacity. To quantitatively evaluate the capacitive contribution of TTFTTA-PDA anodes, normalized contribution ratios of the pseudocapacitive process to the total capacity were calculated to be 33 %, 39 %, 45 %, 49 %, and 52 % at the scan rates of 2.0, 4.0, 6.0, 8.0, and 10.0 mV s^{-1}, respectively (Fig. 4c and d). This result illustrated that the capacity of TTFTTA-PDA anodes was simultaneously contributed by both pseudocapacitive processes (accounting for the superior rate capability) and intercalation reactions (contributing to the high capacity). The Li^+ diffusion coefficient (D_{Li^+}) of TTFTTA-PDA anodes was evaluated by the galvanostatic intermittent titration technique (GITT). The charged and discharged GITT curves were measured at a current density of 20 mA g^{-1} for 20 min followed by a rest time of 30 min to reach the steady-state voltage (Fig. 4e). During the lithiation process, the D_{Li^+} increased from 1.40×10^{-10} to 4.56×10^{-9} cm^2 s^{-1} with the decrease of discharge voltage from 0.94 to 0.06 V (Fig. 4f). During the delithiation process, the D_{Li^+} varied with charge state in the range of 1.11×10^{-8} to 3.16×10^{-10} cm^2 s^{-1}. The D_{Li^+} of TTFTTA-PDA active material was three orders of magnitude higher than that of graphite, which was greatly conducive to overcoming the imbalance issues of the electrochemical kinetics between the battery-type anodes and capacitor-type cathodes in HLICs, achieving the construction of high-power-density HLICs.

In view of the outstanding electrochemical performances of TTFTTA-PDA anodes in half batteries, full-cell HLICs based on TTFTTA-PDA anodes and AC cathodes were assembled to further verify the feasibility and practicality of TTFTTA-PDA anodes. Fig. 5a showed the CV curves of TTFTTA-PDA||AC HLICs at different scan rates from 2.0 to 25.0 mV s^{-1}. The quasi-rectangular current responses in CV curves indicated the electrochemical kinetics balance of the TTFTTA-PDA anodes and AC cathodes. Fig. 5b presented the galvanostatic charge/discharge voltage profiles of TTFTTA-PDA||AC HLICs in the range of 2.0-4.0 V at different current densities. The nearly triangular voltage profiles suggested ideal capacitive behavior of HLICs. Notably, a charge/discharge cycle could be accomplished within 67 s at the current density of 4000 mA g^{-1}, demonstrating an excellent rate capability of TTFTTA-PDA||AC HLICs. The calculation of specific capacitances under different current densities also supported the above conclusion. As shown in Fig. 5c, the areal capacitances of TTFTTA-PDA||AC HLICs were as high as 100.2, 90.5, 82.5, 76.2, 70.9, and 65.1 mF cm^{-2} at 100, 200, 500, 1000, 2000, and 4000 mA g^{-1}, respectively, showcasing enormous practical potential, which was mainly benefited from the fast transport of ions and electrons within the TTFTTA-PDA active material. The Ragone plot of TTFTTA-PDA||AC HLICs was obtained by calculating the energy density and power density at different current densities (Fig. 5d). TTFTTA-PDA||AC HLICs exhibited a good balance between energy density and power density, delivering a high energy density of 140 Wh kg^{-1} at 233 W kg^{-1} and a high power density of 9328 W kg^{-1} at 91 Wh kg^{-1}, demonstrating that the HLICs had a synergistic advantage of combining lithium-ion batteries (LIBs) and electrochemical capacitors (ECs). The long-term cycling stability of TTFTTA-PDA||AC HLICs was evaluated at a high current density of 4000 mA g^{-1} (Fig. 5e), displaying a high capacity retention of 81.3 % after 2200 cycles. The outstanding energy density, power density, and cycling lifespan of the TTFTTA-PDA||AC HLICs were competitive among the reported state-of-the-art HLICs with MOF-/COF-based anode materials (Table S3).

3. Conclusion

In summary, to enhance the performance of HLICs, we have successfully designed a novel electroactive thiophene-linked COF, TTFTTA-PDA-COF. This COF exhibits a high surface area (457 m^2 g^{-1}), excellent chemical and thermal stability, and enhances charge transfer capability. When used as an anode material without any additives, the pristine TTFTA-PDA-COF demonstrates excellent electrochemical performances attributed to the superiorities of COFs and redox-active TTF cores. In half-battery measurements, TTFTTA-PDA-COF anodes show specific capacities from 577.9 mAh g^{-1} to 174.6 mAh g^{-1} at current densities from 200 mA g^{-1} to 3000 mA g^{-1} and high stability corresponding to a capacity retention of 89.5 % after 400 cycles. In full-battery measurements, TTFTTA-PDA||AC HLICs exhibit high energy density of 140 Wh kg^{-1} at 233 W kg^{-1}, high power density of 9328 W kg^{-1} at 91 Wh kg^{-1}, and excellent cycling lifespan according to the capacity retention of 81.3 % after 2200 cycles, and these results are better than other reported advanced HLICs with MOF-/COF-based anode materials. We expect this work can provide new inspiration to the precise design of COFs applying in electrochemical energy storage systems.

4. Experimental section/methods

4.1. Synthesis of TTFTTA-PDA

TTFTTA (10 mg, 0.0155 mmol) and *p*-phenylenediamine (3.4 mg,

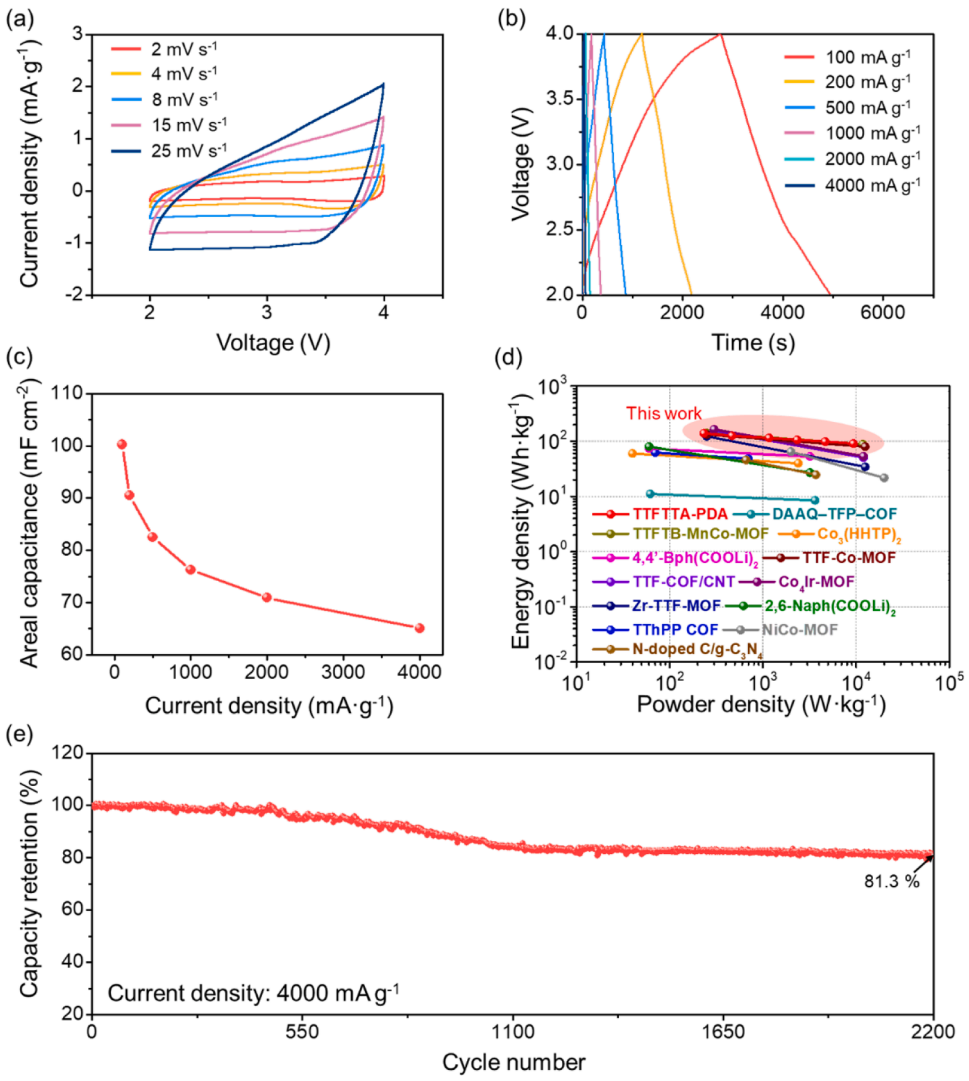

Fig. 5. Electrochemical performance of TTFTTA-PDA||AC HLICs. (a) CV curves of TTFTTA-PDA||AC HLICs between 2.0 and 4.0 V at various scan rates from 2 to 25 mV s^{-1}. (b) Galvanostatic charge/discharge curves of HLICs at different current densities from 100 to 4000 mA g^{-1}. (c) Areal capacitances of TTFTTA-PDA||AC HLICs at different current densities from 100 to 4000 mA g^{-1}. (d) Ragone plots of TTFTTA-PDA||AC HLICs. (e) Long-term cycling stability of TTFTTA-PDA||AC HLICs at a current density of 4000 mA g^{-1}.

0.031 mmol) were charged into a 10 mL Pyrex tube. Then, a mixture of orthodichlorobenzene and 6 M HOAc (1.2 mL, 1/0.2 by vol) was added to the tube, and the mixture was sonicated for 10 min. The resulting mixture was degassed by freeze−pump−thaw cycles and sealed under vacuum. The sealed tube was heated at 120°C for 7 days. The solid was collected by centrifugation and washed with methanol and THF. TTFTTA-PDA was then washed with THF in a Soxhlet extractor overnight. The resulting powder was dried at 100°C under vacuum to yield TTFTTA-PDA (10.5 mg, 62 % yield).

4.2. Electrochemical measurements

To prepare the TTFTTA-PDA anodes, 70 wt.% of TTFTTA-PDA powder, 20 wt.% conductive carbon black additive (Ketjen Black), and 10 wt.% of polyvinylidene fluoride (PVDF) were mixed in N-Methyl pyrrolidone (NMP) solvent to form a slurry. After magnetic stirring for 6 h, the homogeneous slurry was evenly spread onto a copper (Cu) foil by doctor-blade method and dried under vacuum at 100°C overnight. Then, the electrode was punched into small disks with a diameter of 13 mm. Similarly, the AC cathodes were prepared by coating the mixture of AC powder/Ketjen Black/PVDF (8:1:1 in mass) slurry on aluminum (Al) foils.

The coin cells (CR2032 type) were assembled in an Ar-filled glovebox with H_2O and O_2 levels < 0.1 ppm. The electrolyte was 1.0 M $LiPF_6$ in ethylene carbonate/diethyl carbonate (EC/DEC, 1:1 in volume) mixture. For the assembly of TTFTTA-PDA||Li half batteries, TTFTTA-PDA anodes were used as working electrodes, and Li foils were used as counter electrodes. The areal mass loading of TTFTTA-PDA anodes in half batteries were 1.0 mg cm^{-2}. For the assembly of TTFTTA-PDA||AC HLICs, TTFTTA-PDA anodes needed to be prelithiated by adding 100 μL of electrolyte and then directly contacting with a piece of Li foil for 24 h in an Ar-filled glovebox. In the HLICs, the areal mass loadings of AC cathodes and TTFTTA-PDA anodes were 1.5 and 0.5 mg cm^{-2}, respectively. All batteries were cycled on a LAND-CT2001 8-channel battery tester.

Electrochemical impedance spectroscopy (EIS) test of TTFTTA-PDA||Li half batteries was performed in the frequency range from 100 kHz to 100 mHz with an amplitude of 5 mV. Cyclic voltammetry (CV) curves of TTFTTA-PDA||Li half batteries and TTFTTA-PDA||AC HLICs were measured within the voltage range of 0.001-3.0 V and 2.0-4.0 V, respectively. All electrochemical tests mentioned above were performed on a Chenhua CHI-760 electrochemical workstation.

The contributions of capacitive-controlled and diffusion-controlled processes to the specific capacity were estimated by the calculation of *b*-value according to the following equations:

$$i = av^b \tag{1}$$

$$\log i = b\log v + \log a \tag{2}$$

where i is the current response, v is the scan rate, a and b are the adjustable parameters. The b-value could be determined by linearly fitting log$i$ versus log$v$. If $b = 0.5$, it indicated a semi-infinite diffusion process controlled by Li^+ intercalation. If $b = 1.0$, it illustrated a capacitive behavior caused by surface redox reactions. Therefore, for the active materials with an apparent pseudocapacitive behavior, the peak current (i) varied linearly with the scan rate (v).

The capacitive contribution can be quantified according to the Dunn equation:

$$i = k_1 v + k_2 v^{1/2} \tag{3}$$

$$iv^{-1/2} = k_1 v^{1/2} + k_2 \tag{4}$$

where k_1 and k_2 are constants, and the current response i is equal to the sum of capacitive contribution ($k_1 v$) and diffusion-controlled contribution ($k_2 v^{1/2}$). The constants of k_1 and k_2 could be determined by linearly fitting $iv^{-1/2}$ versus $v^{1/2}$.

To calculate Li^+ diffusion coefficient (D_{Li^+}), the galvanostatic intermittent titration technique (GITT) test was performed at the current density of 20 mA g^{-1} for 20 min followed by a rest time of 30 min to reach the steady-state voltage. The D_{Li^+} obtained from GITT was calculated according to the following equation:

$$D_{Li^+} = \frac{4}{\pi\tau}\left(\frac{mV}{MS}\right)^2\left(\frac{\Delta E_s}{\Delta E_t}\right)^2 = \frac{4}{\pi\tau}\left(\frac{m}{\rho S}\right)^2\left(\frac{\Delta E_s}{\Delta E_t}\right)^2 \tag{5}$$

where τ is the pulse time; m, V, M, and ρ are the mass loading, molar volume, molar mass, and density of the active materials, respectively; S is the surface area of electrodes; ΔE_s is the voltage difference between the steady state and the initial state of every step; ΔE_t is the voltage change during a pulse step excluding the iR drop. The density of TTFTTA-PDA was 0.31 g cm^{-3}, which was calculated by measuring the mass and the volume of a pressed TTFTTA-PDA pellet.

The cell-discharge capacitance (C_{cell}) and the specific capacitance (C_s) of HLICs were calculated with the following equations:

$$\Delta V = (V_{max} + V_{min})/2 \tag{6}$$

$$C_{cell} = it/\Delta V \tag{7}$$

$$C_s = C_{cell}/S \tag{8}$$

where i is the applied current, t is the discharging time, V_{max} and V_{min} are the voltages at the beginning and the end of discharge steps, ΔV is the voltage range, and S is the surface area of electrodes.

The energy density (E) and power density (P) were calculated according to the following equations:

$$P = \Delta V \times \frac{i}{m} \tag{9}$$

$$E = P \times t \tag{10}$$

where i is the discharge current, t is the discharge time, ΔV is the voltage range, m is the total loading mass of active materials on the AC cathodes and TTFTTA-PDA anodes.

4.3. Computational method

We performed density functional theory (DFT) calculations using the Vienna Ab-initio Simulation Package (VASP) package with Projector Augmented Wave (PAW) pseudo-potentials. The exchange-correlation energy of the electrons was described by employing the Generalized Gradient Approximations (GGA) using the Perdew-Burke-Ernzerhof (PBE) function. For all calculations in this work, the cutoff energy of the plane wave was set to be 520 eV. The convergence criteria for energy and force are set to be less than 10^{-5} eV and 0.02 eV·$Å^{-1}$. For the k-points sampling of Brillouin-zone integrals, the Monkhorst-Pack grids were set to be 1 × 1 × 1.

CCDC 2365486 (TTFTTA) contain the supplementary crystallographic data for this paper. These data can be obtained free of charge from The Cambridge Crystallographic Data Centre via www.ccdc.cam.ac.uk/data_request/cif.

CRediT authorship contribution statement

Zhi-Mei Yang: Writing – original draft, Validation, Software, Methodology, Investigation, Data curation. **Yaoda Wang:** Writing – original draft, Software, Methodology, Investigation, Data curation. **Meng-Hang Zhang:** Software, Investigation. **Zhe-Yuan Hou:** Validation, Software, Data curation. **Shu-Peng Zhao:** Software, Investigation, Data curation. **Xiao Han:** Validation, Software. **Shuai Yuan:** Writing – review & editing, Validation, Software, Investigation. **Jian Su:** Writing – review & editing, Writing – original draft, Supervision, Project administration, Funding acquisition, Conceptualization. **Zhong Jin:** Writing – review & editing, Writing – original draft, Supervision, Project administration, Funding acquisition, Conceptualization. **Jing-Lin Zuo:** Writing – review & editing, Writing – original draft, Supervision, Project administration, Funding acquisition, Conceptualization.

Declaration of competing interest

The authors declare that they have no known competing financial interests or personal relationships that could have appeared to influence the work reported in this paper.

Acknowledgements

This work was supported by the National Natural Science Foundation of China (Grant No. 22275084, 22301135, 22479074, and 22475096), the General Project of the Joint Fund of Equipment Pre-research and the Ministry of Education (8091B02052407), the Natural Science Foundation of Jiangsu Province (BK20243010, BK20220928, BK20240400 and BK20241236), the Science and Technology Major Project of Jiangsu Province (BG2024013), the Scientific and Technological Innovation Special Fund for Carbon Peak and Carbon Neutrality of Jiangsu Province (BK20220008), the Scientific and Technological Achievements Transformation Special Fund of Jiangsu Province (BA2023037), the Key Core Technology "Open Competition" Project of Suzhou City (SYG2024122), the Gusu Leading Talent Program of Scientific and Technological Innovation and Entrepreneurship of Wujiang District in Suzhou City (ZXL2021273), and the Chenzhou National Sustainable Development Agenda Innovation Demonstration Zone Provincial Special Project (2023sfq11). We thank for the staff from BL17B beamline of National Facility for Protein Science in Shanghai (NFPS) at Shanghai Synchrotron Radiation Facility, for assistance during data collection.

Supplementary materials

Supplementary material associated with this article can be found, in the online version, at doi:10.1016/j.ensm.2025.104038.

Data availability

Data will be made available on request.

References

[1] H. Wang, C. Zhu, D. Chao, Q. Yan, H.J. Fan, Nonaqueous hybrid lithium-ion and sodium-ion capacitors, Adv. Mater. 29 (46) (2017) 1702093.

[2] S. Dong, N. Lv, Y. Wu, G. Zhu, X. Dong, Lithium-ion and sodium-ion hybrid capacitors: from insertion-type materials design to devices construction, Adv. Funct. Mater. 31 (21) (2021) 2100455.

[3] J. Yan, Q. Wang, T. Wei, Z. Fan, Recent advances in design and fabrication of electrochemical supercapacitors with high energy densities, Adv. Energy Mater. 4 (4) (2013) 1300816.

[4] J. Ding, W. Hu, E. Paek, D. Mitlin, Review of hybrid ion capacitors: from aqueous to lithium to sodium, Chem. Rev. 118 (14) (2018) 6457–6498.

[5] J. Zhao, H. Lai, Z. Lyu, Y. Jiang, K. Xie, X. Wang, Q. Wu, L. Yang, Z. Jin, Y. Ma, et al., Hydrophilic hierarchical nitrogen-doped carbon nanocages for ultrahigh supercapacitive performance, Adv. Mater. 27 (23) (2015) 3541–3545.

[6] Z.-S. Wu, W. Ren, L. Wen, L. Gao, J. Zhao, Z. Chen, G. Zhou, F. Li, H.-M. Cheng, Graphene anchored with Co3O4 nanoparticles as anode oflithium ion batteries with enhanced reversible capacity and cyclic performance, ACS Nano (4) (2010) 3187–3194.

[7] G. Zhu, T. Chen, L. Wang, L. Ma, Y. Hu, R. Chen, Y. Wang, C. Wang, W. Yan, Z. Tie, et al., High energy density hybrid lithium-ion capacitor enabled by Co3ZnC@N-doped carbon nanopolyhedra anode and microporous carbon cathode, Energy Storage Mater 14 (2018) 246–252.

[8] L. Zhai, G. Li, X. Yang, S. Park, D. Han, L. Mi, Y. Wang, Z. Li, S.Y. Lee, 30 Li+-Accommodating covalent organic frameworks as ultralong cyclable high-capacity li-ion battery electrodes, Adv. Funct. Mater. 32 (9) (2021) 2108798.

[9] L. Kong, M. Liu, H. Huang, Y. Xu, X.H. Bu, Metal/covalent-organic framework based cathodes for metal-ion batteries, Adv. Energy Mater. 12 (4) (2021) 2100172.

[10] J. Li, X. Jing, Q. Li, S. Li, X. Gao, X. Feng, B. Wang, Bulk COFs and COF nanosheets for electrochemical energy storage and conversion, Chem. Soc. Rev. 49 (11) (2020) 3565–3604.

[11] S.-Y. Ding, W. Wang, Covalent organic frameworks (COFs): from design to applications, Chem. Soc. Rev. 42 (2) (2013) 548–568.

[12] F. Xu, H. Xu, X. Chen, D. Wu, Y. Wu, H. Liu, C. Gu, R. Fu, D. Jiang, Radical covalent organic frameworks: a general strategy to immobilize open-accessible polyradicals for high-performance capacitive energy storage, Angew. Chem. Int. Ed. 54 (23) (2015) 6814–6818.

[13] S. Haldar, P. Bhauriyal, A.R. Ramuglia, A.H. Khan, S. De Kock, A. Hazra, V. Bon, D. L. Pastoetter, S. Kirchhoff, L. Shupletsov, et al., Sulfide-bridged covalent quinoxaline frameworks for lithium–organosulfide batteries, Adv. Mater. 35 (16) (2023) 2210151.

[14] H. Yang, S. Zhang, L. Han, Z. Zhang, Z. Xue, J. Gao, Y. Li, C. Huang, Y. Yi, H. Liu, et al., High conductive two-dimensional covalent organic framework for lithium storage with large capacity, ACS Appl. Mater. Interfaces 8 (8) (2016) 5366–5375.

[15] W. Yan, F. Yu, Y. Jiang, J. Su, S.-W. Ke, Z. Tie, J.-L. Zuo, Z. Jin, Self-assembly construction of carbon nanotube network-threaded tetrathiafulvalene-bridging covalent organic framework composite anodes for high-performance hybrid lithium-ion capacitors, Small Struct 3 (10) (2022) 2200126.

[16] Z.M. Yang, S.P. Zhao, M.H. Zhang, Z.D. Zhang, T.R. Ma, S. Yuan, J. Su, C.H. Li, J. L. Zuo, Coordination-modulated metal tetrathiafulvalene octacarboxylate frameworks for high-performance lithium-ion battery anodes, Angew. Chem. Int. Ed. 62 (27) (2023) e202304183.

[17] Y.-G. Weng, Z.-H. Ren, Z.-R. Zhang, J. Shao, Q.-Y. Zhu, J. Dai, Tetrathiafulvalene–cobalt metal–organic frameworks for lithium-ion batteries with superb rate capability, Inorg. Chem. 60 (22) (2021) 17074–17082.

[18] W. Yan, J. Su, Z.-M. Yang, S. Lv, Z. Jin, J.-L. Zuo, High-performance lithium-ion capacitors based on porosity-regulated zirconium metal-organic frameworks, Small 17 (22) (2020) 2005209.

[19] Z.-H. Ren, Z.-R. Zhang, L.-J. Ma, C.-Y. Luo, J. Dai, Q.-Y. Zhu, Oxidatively doped tetrathiafulvalene-based metal–organic frameworks for high specific energy of supercapatteries, ACS Appl. Mater. Interfaces 15 (5) (2023) 6621–6630.

[20] L.-J. Ma, C.-Y. Luo, R.-N. Wang, Y.-C. Tan, J.-L. Hou, Q.-Y. Zhu, A tetrathiafulvalene-based bimetal–organic framework for a hybrid lithium-ion capacitor: the role of bimetallic centers in charge storage and stability, ACS Energy Lett 8 (10) (2023) 4427–4437.

[21] C. Zhang, Y. He, P. Mu, X. Wang, Q. He, Y. Chen, J. Zeng, F. Wang, Y. Xu, J. X. Jiang, Toward high performance thiophene-containing conjugated microporous polymer anodes for lithium-ion batteries through structure design, Adv. Funct. Mater. 28 (4) (2017) 1705432.

[22] L. Zhan, Z. Song, N. Shan, J. Zhang, J. Tang, H. Zhan, Y. Zhou, Z. Li, C. Zhan, Poly (tetrahydrobenzodithiophene): high discharge specific capacity as cathode material for lithium batteries, J. Power Sources 193 (2) (2009) 859–863.

[23] Y. Liu, H. Zhang, H. Yu, Z. Liao, S. Paasch, S. Xu, R. Zhao, E. Brunner, M. Bonn, H. I. Wang, et al., A thiophene backbone enables two-dimensional Poly(arylene vinylene)s with high charge carrier mobility, Angew. Chem. Int.l Ed. 62 (35) (2023) e202305978.

[24] A. Yoshimura, H. Kimura, K. Kagawa, M. Yoshioka, T. Itou, D. Vasu, T. Shirahata, H. Yorimitsu, Y. Misaki, Synthesis and properties of tetrathiafulvalenes bearing 6-aryl-1,4-dithiafulvenes, Beilstein J. Org. Chem. 16 (2020) 974–981.

[25] T.R. Ma, F. Ge, S.W. Ke, S. Lv, Z.M. Yang, X.C. Zhou, C. Liu, X.J. Wu, S. Yuan, J. L. Zuo, Accessible tetrathiafulvalene moieties in a 3D covalent organic framework for enhanced near-infrared photo-thermal conversion and photo-electrical response, Small 20 (14) (2023) 2308013.

[26] S.-W. Ke, Y. Wang, J. Su, K. Liao, S. Lv, X. Song, T. Ma, S. Yuan, Z. Jin, J.-L. Zuo, Redox-active covalent organic frameworks with Nickel–Bis(dithiolene) units as guiding layers for high-performance lithium metal batteries, J. Am. Chem. Soc. 144 (18) (2022) 8267–8277.

[27] S. Lv, X. Ma, S. Ke, Y. Wang, T. Ma, S. Yuan, Z. Jin, J.-L. Zuo, Metal-coordinated covalent organic frameworks as advanced bifunctional hosts for both sulfur cathodes and lithium anodes in lithium–sulfur batteries, J. Am. Chem. Soc. 146 (13) (2024) 9385–9394.

[28] S. Karak, K. Koner, A. Karmakar, S. Mohata, Y. Nishiyama, N.T. Duong, N. Thomas, T.G. Ajithkumar, M.S. Hossain, S. Bandyopadhyay, et al., Morphology tuning via linker modulation: metal-free covalent organic nanostructures with exceptional chemical stability for electrocatalytic water splitting, Adv. Mater. 36 (12) (2024) 2209919.

[29] A. Sadhukhan, A. Karmakar, K. Koner, S. Karak, R.K. Sharma, A. Roy, P. Sen, K. K. Dey, V. Mahalingam, B. Pathak, et al., Functionality modulation toward thianthrene-based metal-free electrocatalysts for water splitting, Adv. Mater. 36 (18) (2024) 2310938.

[30] H. Ding, Y. Li, H. Hu, Y. Sun, J. Wang, C. Wang, C. Wang, G. Zhang, B. Wang, W. Xu, et al., A tetrathiafulvalene-based electroactive covalent organic framework, Chem. Eur. J. 20 (45) (2014) 14614–14618.

[31] C.F. Leong, C.-H. Wang, C.D. Ling, D.M D'Alessandro, A spectroscopic and electrochemical investigation of a tetrathiafulvalene series of metal–organic frameworks, Polyhedron 154 (2018) 334–342.

[32] J. Su, W. He, X.-M. Li, L. Sun, H.-Y. Wang, Y.-Q. Lan, M. Ding, J.-L. Zuo, High electrical conductivity in a 2D MOF with intrinsic superprotonic conduction and interfacial pseudo-capacitance, Matter 2 (3) (2020) 711–722.

[33] J. Su, P. Cai, T. Yan, Z.-M. Yang, S. Yuan, J.-L. Zuo, H.-C. Zhou, Enhancing the photothermal conversion of tetrathiafulvalene-based MOFs by redox doping and plasmon resonance, Chem. Sci. 13 (6) (2022) 1657–1664.

[34] S. Zhang, D.K. Panda, A. Yadav, W. Zhou, S. Saha, Effects of intervalence charge transfer interaction between π-stacked mixed valent tetrathiafulvalene ligands on the electrical conductivity of 3D metal-organic frameworks, Chem. Sci. 12 (40) (2021) 13379–13391.

[35] J. Su, N. Xu, R. Murase, Z.-M. Yang, D.M. D'Alessandro, J.-L. Zuo, J Zhu, Persistent radical tetrathiafulvalene-based 2D metal-organic frameworks and their application in efficient photothermal conversion, Angew. Chem., Int. Ed. 60 (9) (2021) 4789–4795.

[36] J. Su, T.-H. Hu, R. Murase, H.-Y. Wang, D.M. D'Alessandro, M. Kurmoo, J.-L Zuo, Redox activities of metal–organic frameworks incorporating rare-earth metal chains and tetrathiafulvalene linkers, Inorg. Chem 58 (6) (2019) 3698–3706.

[37] J. Su, S. Yuan, H.-Y. Wang, L. Huang, J.-Y. Ge, E. Joseph, J. Qin, T. Cagin, J.-L. Zuo, H.-C. Zhou, Redox-switchable breathing behavior in tetrathiafulvalene-based metal–organic frameworks, Nat. Commun. 8 (1) (2017) 1–8.

[38] S.-L. Cai, Y.-B. Zhang, A.B. Pun, B. He, J. Yang, F.M. Toma, I.D. Sharp, O.M. Yaghi, J. Fan, S.-R. Zheng, et al., Tunable electrical conductivity in oriented thin films of tetrathiafulvalene-based covalent organic framework, Chem. Sci. 5 (12) (2014) 4693–4700.

[39] B. Ding, M.B. Solomon, C.F. Leong, D.M D'Alessandro, Redox-active ligands: Recent advances towards their incorporation into coordination polymers and metal-organic frameworks, Coord. Chem. Rev. (2021) 439.

[40] Y. Zheng, T. Qian, H. Ji, X. Xia, J. Liu, Y. Zhu, C. Yan, Accelerating ion dynamics under cryogenic conditions by the amorphization of crystalline cathodes, Adv. Mater. 33 (35) (2021) 2102634.